

Tunable magneto-optical effect, anomalous Hall effect, and anomalous Nernst effect in the two-dimensional room-temperature ferromagnet 1T-CrTe₂

Xiuxian Yang^{1,2}, Xiaodong Zhou,¹ Wanxiang Feng^{1,*}, and Yugui Yao¹

¹Key Laboratory of Advanced Optoelectronic Quantum Architecture and Measurement, Ministry of Education, School of Physics, Beijing Institute of Technology, Beijing 100081, China

²Kunming Institute of Physics, Kunming 650223, China



(Received 31 October 2020; revised 31 December 2020; accepted 8 January 2021; published 21 January 2021)

Utilizing first-principles density functional theory calculations together with group theory analyses, we systematically investigate the spin-order-dependent magneto-optical effect (MOE), anomalous Hall effect (AHE), and anomalous Nernst effect (ANE) in the recently discovered two-dimensional room-temperature ferromagnet 1T-CrTe₂. We find that the spin prefers an in-plane direction by the magnetocrystalline anisotropy energy calculations. The MOE, AHE, and ANE display a period of $2\pi/3$ when the spin rotates within the atomic plane, and they are forbidden if a mirror plane perpendicular to the spin direction exists. By reorienting the spin from the in-plane to out-of-plane direction, the MOE, AHE, and ANE are enhanced by around one order of magnitude. Moreover, we establish the layer-dependent magnetic properties of multilayer 1T-CrTe₂ and predict antiferromagnetism and ferromagnetism for bilayer and trilayer 1T-CrTe₂, respectively. The MOE, AHE, and ANE are prohibited in antiferromagnetic bilayer 1T-CrTe₂ due to the existence of the space-time inversion symmetry, whereas all of them are activated in ferromagnetic trilayer 1T-CrTe₂ and are significantly enhanced compared to those of monolayer 1T-CrTe₂. Our results show that the magneto-optical and anomalous transports properties of 1T-CrTe₂ can be effectively modulated by altering spin direction and layer number.

DOI: [10.1103/PhysRevB.103.024436](https://doi.org/10.1103/PhysRevB.103.024436)

I. INTRODUCTION

Although two-dimensional (2D) materials have been explored for more than a decade, the magnetic order rarely survives in atomically thin films due to thermal fluctuations [1]. The realization of 2D magnets is a big challenge [2] and has attracted extensive attention [3,4]. The 2D magnetic van der Waals (vdW) materials are especially expected to open up a wide range of possibilities for spintronics [5–7]. Thanks to the improvement of theoretical methods and experimental capabilities, more and more 2D magnetic vdW materials have been discovered, which indicates that the field of 2D magnets is advancing rapidly [8]. In recent years, for example, tens of 2D vdW materials with stable magnetic orders have been observed in layered FePS₃ [9,10], Cr₂Ge₂Te₆ [11], CrX₃ (X=I, Br, Cl) [12–21], Fe₃GeTe₂ [22–24], MX₂ (M=V, Mn; X=Se, Te) [25–27], MnSn [28], PtSe₂ [29], and CrTe₂ [30–32].

Aimed at the application of 2D spintronics, detecting spontaneous magnetization is the primary step. Standard techniques, such as superconducting quantum interference device (SQUID) magnetometer and neutron scattering, are challenging to use for 2D magnetic vdW materials [3,4]. Instead, magneto-optical effects (MOE), represented by the Kerr [33] and Faraday [34] effects, are considered to be a powerful and noncontact (nondestructive) probe of magnetism in 2D materials [11,12]. The magneto-optical Kerr and Faraday effects are defined as the rotation of the polarization planes of

reflected and transmitted light beams when a linearly polarized light hits the magnetic materials [35]. In condensed-matter physics, the MOE and the anomalous Hall effect (AHE) [36], where the latter is characterized by a transverse voltage generated by a longitudinal charge current in the absence of external magnetic fields, are two fundamental phenomena that usually coexist in ferromagnets and antiferromagnets. There are two distinct contributions to the AHE, that is, the extrinsic AHE (i.e., side jump and skew scattering) depending on the scattering of electrons off impurities or due to disorder and the intrinsic AHE expressed in term of Berry curvatures in a perfect crystal [36]. According to the Kubo formula [37,38], the intrinsic anomalous Hall conductivity (AHC) can be straightforwardly extended to the optical Hall conductivity, which is intimately related to the magneto-optical Kerr and Faraday effects [39]. Because of the inherent relationship between the intrinsic AHE and MOE, they are often studied together. Moreover, the transverse charge current can also be generated by a longitudinal temperature gradient, called the anomalous Nernst effect (ANE) [40], which has attracted enormous interest mainly due to its promising application in thermoelectrics. The giant ANE was recently discovered in chiral magnets [41,42] and topological semimetals [43,44].

The catalog of 2D magnetic vdW materials is rich; however, ferromagnetic candidates with high Curie temperatures T_C are still limited, hindering enormously the development of 2D spintronics. Fortunately, a 2D dichalcogenide with the 1T polytype, 1T-CrTe₂ [see Figs. 1(a) and 1(b)], was recently synthesized with an exceptionally high T_C (>300 K)

*wxmfeng@bit.edu.cn

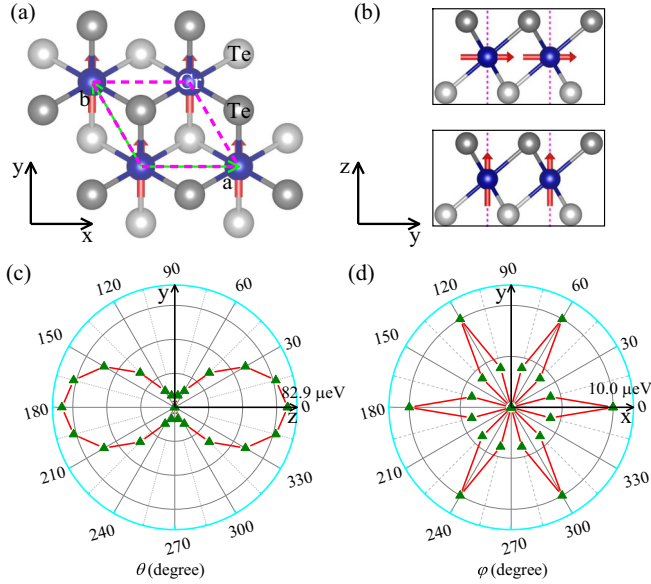


FIG. 1. (a) and (b) Top and side views of monolayer 1T-CrTe₂. The blue spheres represent Cr atoms, whereas dark gray and silver-white spheres represent Te atoms in the upper and lower sublayers. The pink dashed lines draw the 2D primitive cell, and the red arrows indicate the directions of spin magnetic moments. The top and bottom panels in (b) present the spin directions along the y and z axes, respectively. (c) and (d) The magnetocrystalline anisotropy energy of monolayer 1T-CrTe₂ by rotating the spin magnetic moment within the yz and xy planes. The spin along the y axis is set to be the reference state.

[30–32]. In this work, based on the first-principles density functional theory calculations and group theory analyses, we systematically investigate the electronic, magnetic, magneto-optical, and anomalous charge and thermoelectric transports properties of monolayer and multilayer 1T-CrTe₂ (hereafter, we use CrTe₂ for simplification). We find that monolayer CrTe₂ is a ferromagnetic metal with the in-plane magnetization direction. By calculating magnetocrystalline anisotropy energy (MAE), the magnetization direction is finely identified along the y axis [see Fig. 1(a)], and the maximal value of MAE between in-plane and out-of-plane magnetization directions reaches 82.9 $\mu\text{eV}/\text{cell}$. The MOE, AHE, and ANE display a period of $2\pi/3$ by rotating the spin within the xy plane, and they disappear if a mirror plane perpendicular to the spin direction exists. We then show that changing the spin from the in-plane to out-of-plane direction can enhance the MOE, AHE, and ANE by around one order of magnitude. Additionally, the layer-dependent magnetic properties of multilayer CrTe₂ are studied, and antiferromagnetism and ferromagnetism for bilayer and trilayer CrTe₂ are predicted, respectively. For antiferromagnetic bilayer CrTe₂, the MOE, AHE, and ANE are fully suppressed due to the existence of the space-time inversion symmetry \mathcal{TP} (\mathcal{T} and \mathcal{P} are time-reversal and spatial inversion operations, respectively). In contrast, the MOE, AHE, and ANE are activated in ferromagnetic trilayer CrTe₂, and all of them are significantly enhanced compared to those of monolayer CrTe₂. Our results show that the magneto-optical and anomalous transports pro-

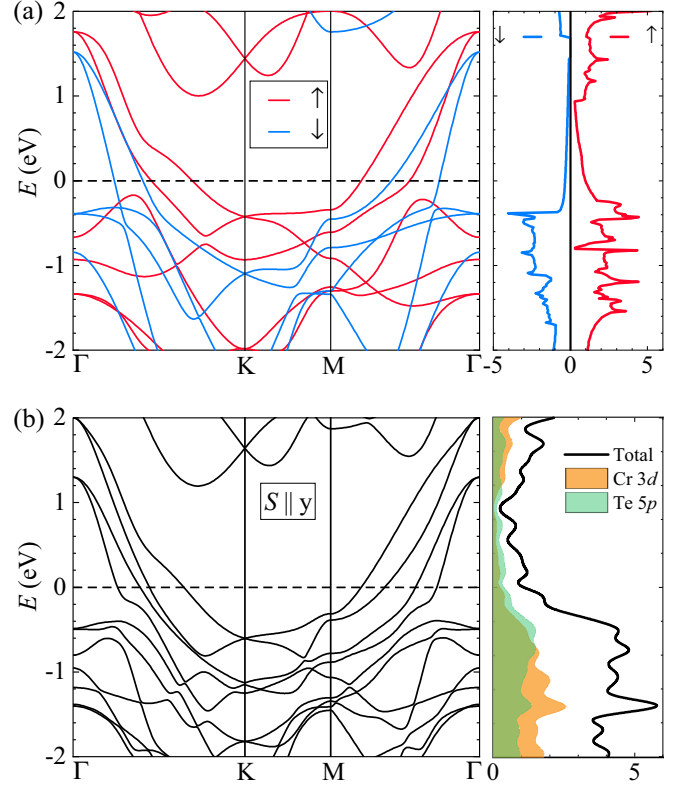


FIG. 2. (a) The spin-polarized band structure and density of states (in units of states/eV per cell) for monolayer 1T-CrTe₂. (b) The relativistic band structure and orbital-decomposed density of states (in units of states/eV per cell) for monolayer 1T-CrTe₂ when the spin is along the y axis.

perties of 2D CrTe₂ are tunable by altering the magnetization direction and the number of layers.

II. METHODOLOGY

The first-principles calculations were performed with the Vienna Ab initio Simulation Package (VASP) [45,46] within the framework of density functional theory. The projector augmented wave method [47] was employed to model the ion cores and the exchange-correlation functional of the generalized gradient approximation (GGA) with the Perdew-Burke-Ernzerhof parametrization (PBE) [48] to simulate the valence electrons. Spin-orbit coupling was included in the calculations of the MAE, MOE, AHE, and ANE. The plane-wave cutoff energy was set to be 500 eV. The structures were relaxed until the maximum force on each atom was less than 0.0001 eV/Å, and the energy convergence criterion was 10^{-7} eV. The Brillouin zone integration was carried out by $16 \times 16 \times 1$ k -point sampling. A vacuum layer with a thickness of at least 15 Å was used to avoid the interactions between adjacent layers, and the vdW correction was adopted by the semiempirical GGA-type density functional constructed with a long-range dispersion correction (DFT-D2 method) in multilayer structures. The optical conductivity, AHC, and anomalous Nernst conductivity (ANC) are scaled by a factor of Z/d_0 to exclude the vacuum region, where Z is the cell length normal to the atomic plane and $d_0 = 6.23$,

TABLE I. The magnetic space group (MSG) and magnetic point group (MPG) of monolayer 1T-CrTe₂ as a function of azimuthal (φ) and polar (θ) angles when the spin rotates within the xy ($\theta = \pi/2$, $0 \leq \varphi \leq \pi$) and yz ($0 \leq \theta \leq \pi$, $\varphi = \pi/2$) planes.

	0°	15°	30°	45°	60°	75°	90°	105°	120°	135°	150°	165°	180°
MSG (φ)	$C2/m$	$P\bar{1}$	$C2'/m'$	$P\bar{1}$	$C2/m$	$P\bar{1}$	$C2'/m'$	$P\bar{1}$	$C2/m$	$P\bar{1}$	$C2'/m'$	$P\bar{1}$	$C2/m$
MPG (φ)	$2/m$	$\bar{1}$	$2'/m'$	$\bar{1}$	$2/m$	$\bar{1}$	$2'/m'$	$\bar{1}$	$2/m$	$\bar{1}$	$2'/m'$	$\bar{1}$	$2/m$
MSG (θ)	$P3m'1$	$C2'/m'$	$C2'/m'$	$C2'/m'$	$C2'/m'$	$C2'/m'$	$C2'/m'$	$C2'/m'$	$C2'/m'$	$C2'/m'$	$C2'/m'$	$C2'/m'$	$P3m'1$
MPG (θ)	$\bar{3}1m'$	$2'/m'$	$2'/m'$	$2'/m'$	$2'/m'$	$2'/m'$	$2'/m'$	$2'/m'$	$2'/m'$	$2'/m'$	$2'/m'$	$2'/m'$	$\bar{3}1m'$

12.46, and 18.69 Å are the effective thicknesses of monolayer, bilayer, and trilayer CrTe₂, respectively. Since the d orbitals of Cr atom are not fully filled, the local-density approximation + U method [49,50] was used to account for the Coulomb correlation with $U = 2.0$ eV [51].

To obtain the MOE, such as the Kerr and Faraday spectra, the optical conductivity should be primarily calculated. Here, we constructed the maximally localized Wannier functions (MLWFs) in a non-self-consistent process by projecting onto s , p , and d orbitals of the Cr atom as well as onto s and p orbitals of the Te atom, using a uniform k mesh of $16 \times 16 \times 1$ points in conjunction with the WANNIER90 package [52]. The optical conductivity was then calculated by integrating the dipole matrix elements (under the MLWF basis) over the entire Brillouin zone using very dense k points of $300 \times 300 \times 1$. The absorptive parts of the optical conductivity are given by [37,38,53]

$$\sigma_{xx}^1(\omega) = \frac{\lambda}{\omega} \sum_{\mathbf{k}, j, j'} [|\Pi_{jj'}^+|^2 + |\Pi_{jj'}^-|^2] \delta(\omega - \omega_{jj'}), \quad (1)$$

$$\sigma_{xx}^2(\omega) = \frac{\lambda}{\omega} \sum_{\mathbf{k}, j, j'} [|\Pi_{jj'}^+|^2 - |\Pi_{jj'}^-|^2] \delta(\omega - \omega_{jj'}), \quad (2)$$

where superscripts 1 and 2 indicate the real and imaginary parts, $\lambda = \frac{\pi e^2}{2\hbar m^2 V}$ is a material-specific constant (e and m are the charge and mass of an electron, \hbar is the reduced Planck constant, and V is the volume of the unit cell), j and j' denote

occupied and unoccupied states at the same k point, $\Pi_{jj'}^\pm$ are the dipole matrix elements relevant to right-circularly (+) and left-circularly (−) polarized lights, $\hbar\omega$ is the photon energy, and $\hbar\omega_{jj'}$ is the energy difference between j and j' states. Utilizing the Kramers-Kronig transformation, the dispersive parts can be obtained as

$$\sigma_{xx}^2(\omega) = -\frac{2}{\pi} \mathcal{P} \int_0^\infty \frac{\sigma_{xx}^1(\omega')}{\omega'^2 - \omega^2} d\omega', \quad (3)$$

$$\sigma_{xy}^1(\omega) = \frac{2}{\pi} \mathcal{P} \int_0^\infty \frac{\omega \sigma_{xy}^2(\omega')}{\omega'^2 - \omega^2} d\omega', \quad (4)$$

where \mathcal{P} is the principal integral.

The Kerr effect is characterized by the rotation angle θ_K and ellipticity ε_K , which are usually combined into the complex Kerr angle,

$$\phi_K = \theta_K + i\varepsilon_K = i \frac{2\omega d}{c} \frac{\sigma_{xy}}{\sigma_{xx}^s}, \quad (5)$$

where c is the speed of light in vacuum, d is the thin-film thickness, and σ_{xx}^s is the optical conductivity of a nonmagnetic substrate. Here, we choose the large band gap insulator SiO₂ to be the nonmagnetic substrate, and $\sigma_{xx}^s = i(1 - n^2)\omega/4\pi$, with refractive index $n = 1.546$. Similarly, the complex Faraday angle is given by

$$\phi_F = \theta_F + i\varepsilon_F = i \frac{\omega d}{2c} (n_+ - n_-), \quad (6)$$

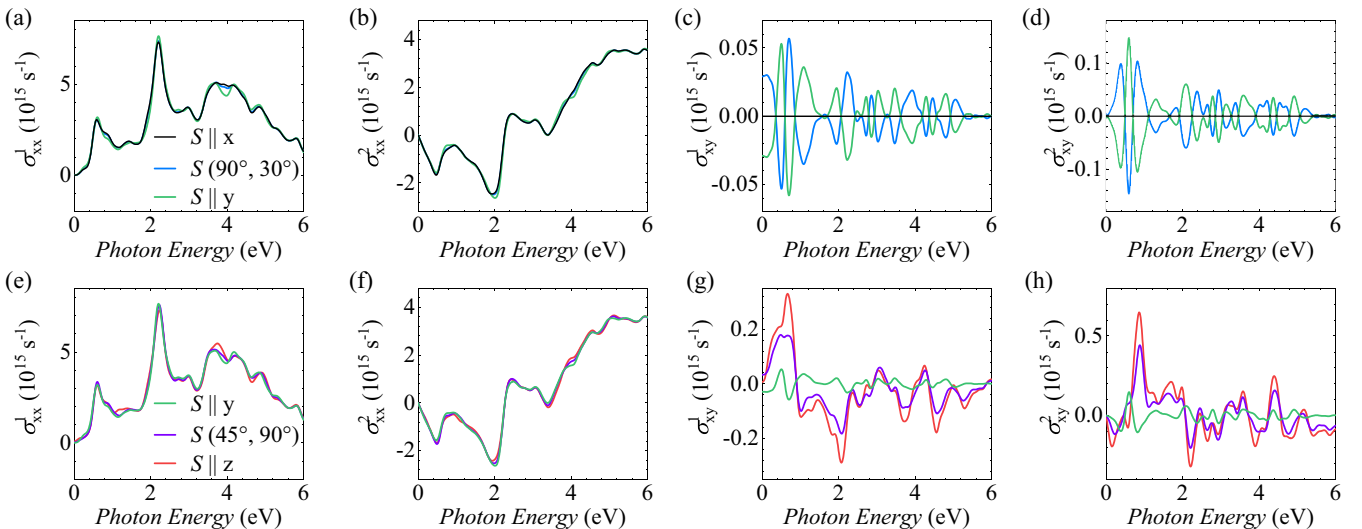


FIG. 3. (a) and (e) The real diagonal, (b) and (f) imaginary diagonal, (c) and (g) real off-diagonal, and (d) and (h) imaginary off-diagonal elements of optical conductivity for monolayer 1T-CrTe₂ with in-plane and out-of-plane magnetization, respectively. For a better comparison, the curves when spin points along the y axis ($S \parallel y$) are replotted in (e)–(h).

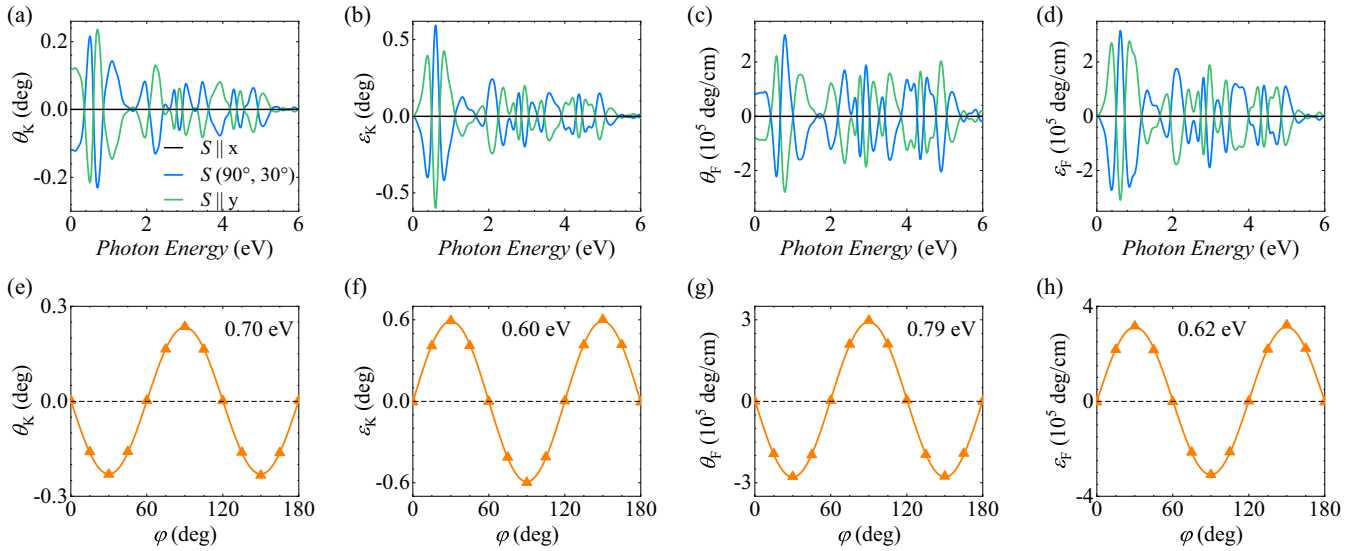


FIG. 4. (a) The Kerr rotation angle θ_K , (b) Kerr ellipticity ε_K , (c) Faraday rotation angle θ_F , and (d) Faraday ellipticity ε_F for monolayer 1T-CrTe₂ with in-plane magnetization. (e)–(h) The Kerr and Faraday rotation angles and ellipticities as a function of azimuthal angle φ at selected photon energies.

where $n_{\pm}^2 = 1 + \frac{4\pi i}{\omega}(\sigma_{xx} \pm i\sigma_{xy})$ are eigenvalues of dielectric tensor. By considering the fact that $|\frac{4\pi i}{\omega}(\sigma_{xx} \pm i\sigma_{xy})| \ll 1$, the complex Faraday angle can be approximately written as

$$\theta_F = \theta_F + i\varepsilon_F \simeq -\frac{2\pi d}{c}\sigma_{xy}. \quad (7)$$

From Eqs. (5) and (7), one can see that the off-diagonal elements of optical conductivity σ_{xy} , also known as the optical Hall conductivity, are determinative of both Kerr and Faraday effects. It should be mentioned here that Eqs. (5)–(7) are expressions for 2D systems with a polar geometry [54]; that is, the incident light propagates along the $-z$ direction.

Physically speaking, the MOE is closely related to the AHE. For example, the dc limit of the real part of the off-diagonal element of optical conductivity, i.e., $\sigma_{xy}^1(\omega \rightarrow 0)$, is nothing but the intrinsic AHC, which can also be calculated from the Berry-phase formula [55],

$$\sigma_{xy}^A = -\frac{e^2}{\hbar V} \sum_{n,\mathbf{k}} f_{n\mathbf{k}} \Omega_{xy}^n(\mathbf{k}), \quad (8)$$

where n , \mathbf{k} , and $f_{n\mathbf{k}}$ are band index, crystal momentum, and Fermi-Dirac distribution function, respectively. $\Omega_{xy}^n(\mathbf{k})$ is the

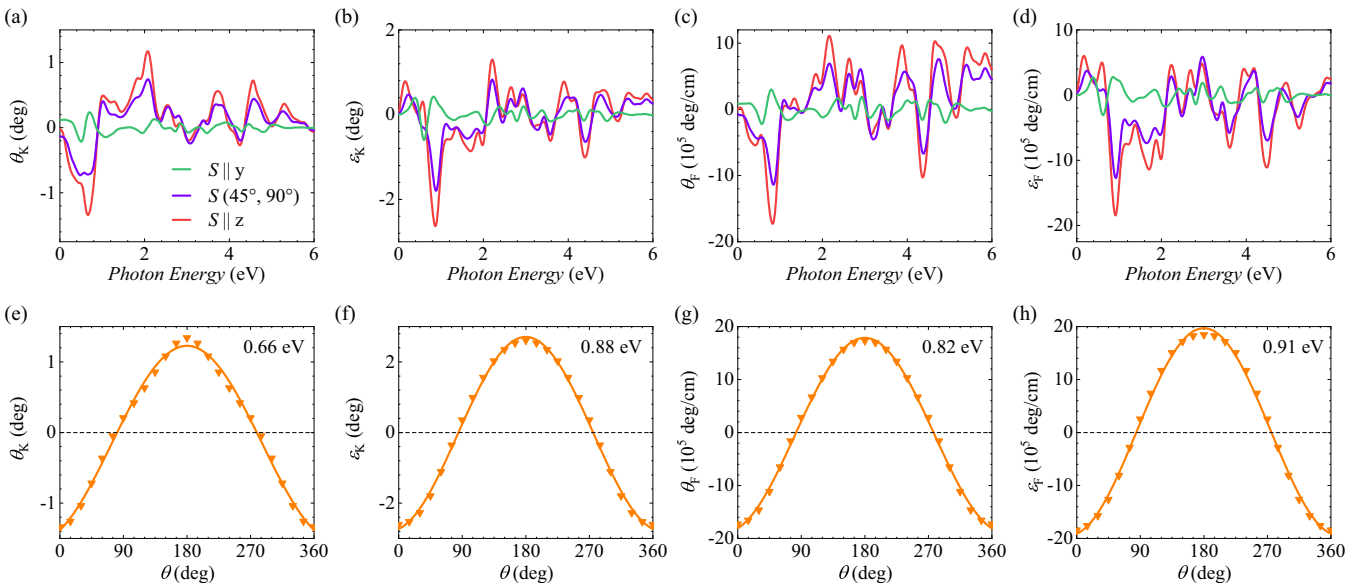


FIG. 5. (a) The Kerr rotation angle θ_K , (b) Kerr ellipticity ε_K , (c) Faraday rotation angle θ_F , and (d) Faraday ellipticity ε_F for monolayer 1T-CrTe₂ with out-of-plane magnetization. For a better comparison, the curves for the spin pointing along the y axis ($S \parallel y$) are also plotted in (a)–(d). (e)–(h) The Kerr and Faraday rotation angles and ellipticities as a function of polar angle θ at selected photon energies.

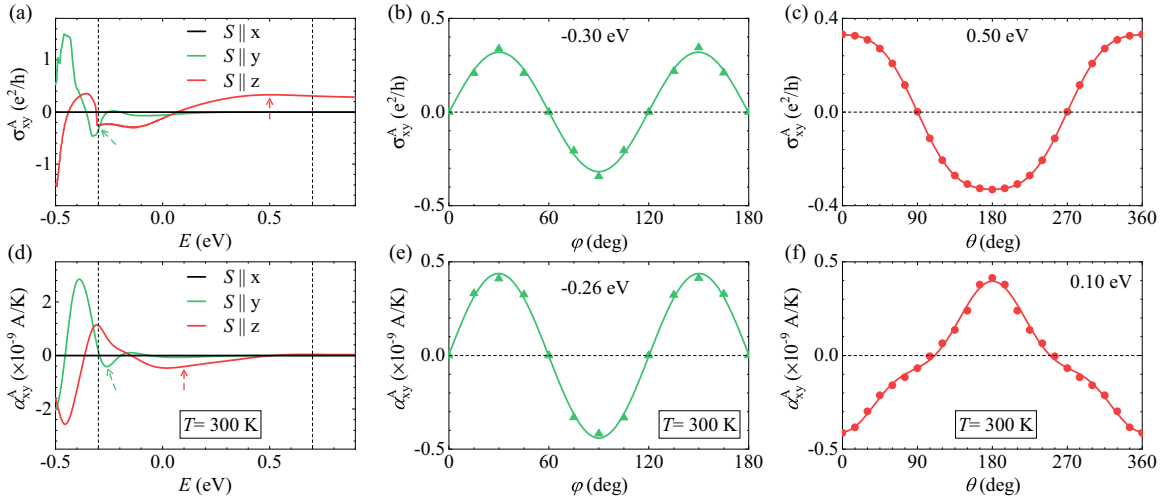


FIG. 6. (a) and (d) The intrinsic anomalous Hall (σ_{xy}^A) and anomalous Nernst (α_{xy}^A) conductivities for monolayer 1T-CrTe₂ as a function of the Fermi energy when the spin points along the x , y , and z axes. α_{xy}^A is calculated at a temperature of 300 K. The vertical dashed lines mark the realistic doping region of 0.31–0.70 eV. The green and red arrows indicate the energies selected for plotting σ_{xy}^A and α_{xy}^A as a function of φ or θ , respectively. (b) and (e) σ_{xy}^A and α_{xy}^A as a function of azimuthal angle φ when the Fermi energies are set to be −0.30 and −0.26 eV, respectively. (c) and (f) σ_{xy}^A and α_{xy}^A as a function of polar angle θ when the Fermi energies are set to be 0.50 and 0.10 eV, respectively.

band-resolved Berry curvature, given by

$$\Omega_{xy}^n(\mathbf{k}) = - \sum_{n' \neq n} \frac{2\text{Im}[\langle \psi_{n\mathbf{k}} | \hat{v}_x | \psi_{n'\mathbf{k}} \rangle \langle \psi_{n'\mathbf{k}} | \hat{v}_y | \psi_{n\mathbf{k}} \rangle]}{(\varepsilon_{n\mathbf{k}} - \varepsilon_{n'\mathbf{k}})^2}, \quad (9)$$

where $\hat{v}_{x,y}$ is the velocity operator along the x or y direction and $\psi_{n\mathbf{k}}$ and $\varepsilon_{n\mathbf{k}}$ are the eigenvector and eigenvalue at band index n and crystal momentum \mathbf{k} , respectively. The intrinsic ANC can be written as [56,57]

$$\alpha_{xy}^A = \frac{e}{\hbar T V} \sum_{n,\mathbf{k}} \Omega_{xy}^n(\mathbf{k}) \times [(\varepsilon_{n\mathbf{k}} - \mu) f_{n\mathbf{k}} + k_B T \ln(1 + e^{-(\varepsilon_{n\mathbf{k}} - \mu)/k_B T})], \quad (10)$$

where T , μ , and k_B are temperature, chemical potential, and Boltzmann constant, respectively. Thus, the ANC can be related to the AHC by the Mott formula [56].

III. RESULTS AND DISCUSSION

In this section, we successively present the results of monolayers and multilayer CrTe₂. The magnetic ground states are first established by calculating the MAE. The corresponding electronic band structures are explicitly calculated. The magnetic group theory is then used to determine the nonzero elements of optical conductivity, which is the critical ingredient to evaluate the magneto-optical Kerr and Faraday spectra. Finally, the anomalous Hall and anomalous Nernst conductivities are evaluated by using the Berry-phase formulas. The dependence of the MOE, AHE, and ANE on the magnetization direction and layer number will be discussed in detail.

A. Monolayer CrTe₂

1. Crystal, magnetic, and electronic structures

The top and side views of monolayer CrTe₂ (space group $P\bar{3}m1$, No. 164) are depicted in Figs. 1(a) and 1(b). Each primitive cell contains one chromium atom and two tellurium

atoms, forming the sandwich structure Te-Cr-Te. The optimized lattice constant of monolayer CrTe₂ is $a = 3.722$ Å.

To confirm the magnetic ground state, we compared total energies among the nonmagnetic, antiferromagnetic, and ferromagnetic states using a supercell of $2 \times 2 \times 1$, and the results show that the ferromagnetic state is more stable than nonmagnetic and antiferromagnetic states by 2.90 eV and 55.32 meV, respectively. Additionally, the magnetic ground state can be determined via the superexchange mechanism [58–60]. The magnetic exchange interactions depend on the filling of the d orbitals of the cations and on the angle formed by the chemical bonds connecting the ligand and magnetic atoms, and particularly, when the angle equals 90°, the ferromagnetic interactions are optimal. In the case of CrTe₂, the bond angle between Cr-Te-Cr is 87°, which accounts for ferromagnetic interactions. Furthermore, the MAE, defined as $\text{MAE}(\theta, \varphi) = E(\theta, \varphi) - E(\theta = 90^\circ, \varphi = 90^\circ)$ [here, $E(\theta, \varphi)$ is the total energy when the spin magnetic moment S orients to the polar angle θ and azimuthal angle φ], is

TABLE II. The total energy E_{tot} (in eV) per unit cell of bilayer (BL) and trilayer (TL) 1T-CrTe₂ with in-plane and out-of-plane ferromagnetic (I-FM [Figs. 7(a) and 7(e)] and O-FM [Figs. 7(c) and 7(g)] and antiferromagnetic (I-AFM [Figs. 7(b) and 7(f)] and O-AFM [Figs. 7(d) and 7(h)]) configurations. The energies of nonmagnetic (NM) structures are given for reference. The relaxed lattice constant a (in Å) is also listed.

	I-FM	O-FM	I-AFM	O-AFM	NM
BL					
E_{tot}	−31.996	−31.983	−32.021	−32.017	−28.885
a	3.763	3.754	3.784	3.786	3.469
TL					
E_{tot}	−48.216	−48.208	−48.238	−48.237	−43.528
a	3.778	3.778	3.791	3.793	3.478

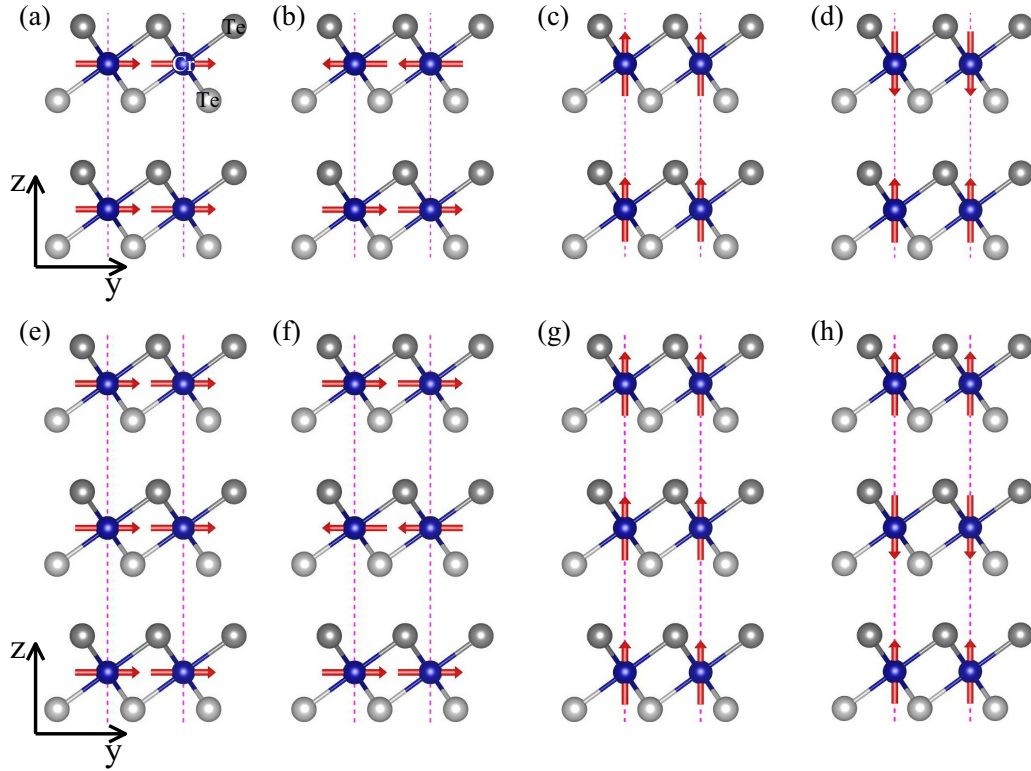


FIG. 7. Side views of (a)–(d) bilayer and (e)–(h) trilayer 1T-CrTe₂ with in-plane and out-of-plane ferromagnetic and antiferromagnetic configurations. The red arrows label the spin directions.

computed by rotating the spin magnetic moment on the xy and yz planes, as shown in Figs. 1(c) and 1(d). The positive values of MAE suggest a preferred magnetization along the y axis ($\theta = 90^\circ$, $\varphi = 90^\circ$) rather than along other directions. Figure 1(c) shows that the out-of-plane magnetization (along the z axis) is not favorable due to the positive MAE of $82.9 \mu\text{eV}/\text{cell}$, which is consistent with the experimental observations of in-plane magnetization for multilayer CrTe₂ ($>8.7 \text{ nm}$) [31,32]. Figure 1(d) further indicates a small in-plane magnetocrystalline anisotropy ($0 \leq \text{MAE} \leq 10.0 \mu\text{eV}/\text{cell}$) with a sixfold symmetry. Due to the small in-plane MAE, sixfold symmetry cannot be systematically observed in experiments, although the 120° magnetic domain walls actually exist in the experimental samples [32]. These results indicate that the in-plane magnetization and sixfold symmetry could still remain from multilayer down to monolayer. Therefore, the magnetic ground state of the system is confirmed, and the spin magnetic moment should be along the y axis, i.e., $S(\theta = 90^\circ, \varphi = 90^\circ)$ or $S \parallel y$ [see top panel of Fig. 1(b)], which is consistent with a previous theoretical calculation [61].

The 2D in-plane ferromagnetic order and the magnetization direction tunability can be concurrently realized in monolayer CrTe₂. On the one hand, the out-of-plane MAE of monolayer CrTe₂ ($82.9 \mu\text{eV}/\text{cell}$) is significantly larger than that of monolayer CrCl₃ ($34 \mu\text{eV}/\text{cell}$) [62]. Since monolayer CrCl₃ was successfully synthesized and its in-plane magnetization was confirmed [63], the 2D in-plane ferromagnetic order is likely established in monolayer CrTe₂ as well. On the other hand, the out-of-plane and in-plane MAEs of monolayer CrTe₂ (82.9 and $10.0 \mu\text{eV}/\text{cell}$) are (much) smaller

than the MAEs of other famous 2D ferromagnets, such as Cr₂Ge₂Te₆ ($\sim 100 \mu\text{eV}/\text{cell}$) [64], CrI₃ ($1.37 \text{ meV}/\text{cell}$) [65], and Fe₃GeTe₂ ($2.76 \text{ meV}/\text{cell}$) [66]. Since the magnetization direction of monolayer Fe₃GeTe₂ has been altered by applying an external magnetic field [66], the tuning of the magnetization direction for monolayer CrTe₂ should be realized more easily. It provides a technical basis for us to reorient the spin magnetic moment within the xy plane and from the xy plane to the z axis [see bottom panel of Fig. 1(b)].

We then discuss the electronic structures of monolayer CrTe₂. Figure 2(a) plots the spin-polarized band structures and density of states, in which the red and blue lines represent the spin-up (\uparrow) and spin-down (\downarrow) bands, respectively. The spin-polarized band structures combined with the density of states clearly show that monolayer CrTe₂ is a ferromagnetic metal. After including spin-orbit coupling, the relativistic band structures and orbital-decomposed density of states with the magnetization $S \parallel y$ are illustrated in Fig. 2(b). The band structure is very consistent with a recent theoretical calculation [67]. For the density of states, we present only the dominant components, i.e., the $3d$ orbitals of the Cr atom (the orange pattern) and $5p$ orbitals of Te atoms (the green pattern), which have nearly equal contributions around the Fermi energy.

2. Magnetic group theory

Group theory is a powerful tool for identifying nonvanishing elements of the optical Hall conductivity, which is the key factor in predicting the MOE. Additionally, the AHE and ANE have the same symmetry requirements as the MOE due to their

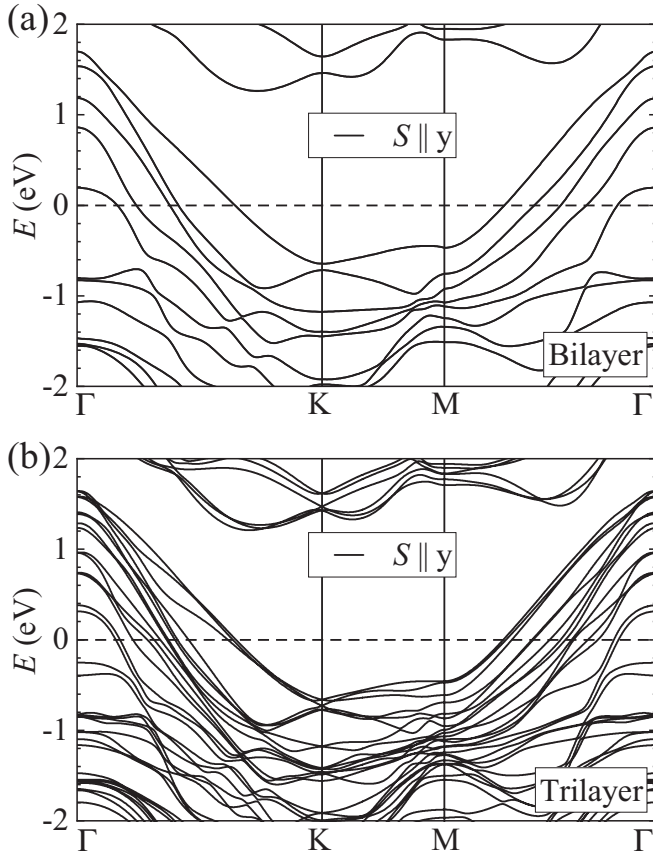


FIG. 8. Relativistic band structures of bilayer and trilayer 1T-CrTe₂ when the spin is along the y axis.

physical relations [refer to Eqs. (1)–(10)]. Hence, we take the optical Hall conductivity as an example, and the results of symmetry analyses are applicable to the MOE, AHE, and ANE. The magnetic space and point groups for monolayer CrTe₂ are calculated by using the ISOTROPY software [68]. Table I lists the results when the spin rotates within the xy and yz planes. Since the optical Hall conductivity is translationally invariant, it is sufficient to restrict the analysis to the magnetic point group. Moreover, the vector-form notation of the optical Hall conductivity, given by $\sigma(\omega) = [\sigma^x, \sigma^y, \sigma^z] = [\sigma_{yz}, \sigma_{zx}, \sigma_{xy}]$, is used for convenience as it can be regarded as a pseudovector, just like spin. Thus, a 2D system always has $\sigma^x = \sigma^y = 0$, and only σ^z is potentially nonzero.

Let us start with the situation of rotating the spin within the xy plane. The magnetic point group has a period of $\pi/3$: $2/m \rightarrow \bar{1} \rightarrow 2'/m' \rightarrow \bar{1} \rightarrow 2/m$, and three nonrepetitive elements are $2/m$, $\bar{1}$, and $2'/m'$. First, group $2/m$ (when $\varphi = n\pi/3$, with $n \in \mathbb{N}$) has a mirror plane that is parallel to the z axis and is perpendicular to the spin direction. Such a mirror operation reverses the sign of σ^z , thus indicating $\sigma^z = 0$. It results in the vanishing optical Hall conductivity, i.e., $\sigma(\omega) = [0, 0, 0]$. On the other hand, all mirror symmetries are broken if $\varphi \neq n\pi/3$. Group $2'/m'$ contains a combined symmetry \mathcal{TM} , where \mathcal{T} is the time-reversal symmetry and \mathcal{M} is a mirror plane that parallels both the z axis and spin direction. Both the \mathcal{T} and \mathcal{M} operations reverse the sign of σ^z , and hence, σ^z is even under \mathcal{TM} symmetry. It gives rise to

the nonvanishing optical Hall conductivity, $\sigma(\omega) = [0, 0, \sigma^z]$. Finally, for group $\bar{1} = \{E, \mathcal{P}\}$, none of its elements (unit operation E and spatial inversion \mathcal{P}) can affect σ^z , and hence, the optical Hall conductivity is absolutely allowed.

We next turn to the case where the spin lies within the yz plane. The evolution of the magnetic point group exhibits a period of π , and only two groups, $\bar{3}1m'$ and $2'/m'$, are needed for the analysis. If $\theta = 0$ or π , group $\bar{3}1m'$ contains three \mathcal{TM} symmetries with $\mathcal{M} \parallel z$. The nonvanishing optical Hall conductivity can be expected since any one of the three \mathcal{TM} symmetries affords $\sigma^z \neq 0$. Once the spin cants away from the z axis ($\theta \neq 0$) or from the $-z$ axis ($\theta \neq \pi$), the magnetic point group changes to $2'/m'$, in which only one of the three \mathcal{TM} symmetry remains (here, \mathcal{M} is just the yz plane) but still ensures $\sigma^z \neq 0$. To summarize, the optical Hall conductivity is nonzero when the spin lies within the yz plane, that is, $\sigma(\omega) = [0, 0, \sigma^z]$.

3. Optical and magneto-optical properties

After obtaining the electronic structures and magnetic groups of monolayer CrTe₂ with different magnetization directions, we now focus on the optical conductivity, which is a prerequisite to evaluate the MOE.

We first discuss the results of in-plane magnetization for $S(90^\circ, 0^\circ)$ ($S \parallel x$), $S(90^\circ, 30^\circ)$, and $S(90^\circ, 90^\circ)$ ($S \parallel y$), shown in Figs. 3(a)–3(d). According to Eqs. (1) and (2), the absorptive parts of optical conductivity, σ_{xx}^1 and σ_{xy}^2 , have direct physical interpretations, which measure the average and difference in absorptions of left- and right-circularly polarized light, respectively. The σ_{xx}^1 plotted in Fig. 3(a) exhibits two sharp absorption peaks at 0.6 and 2.2 eV. Since σ_{xx}^1 is directly related to the interband transition probability and jointed density of states, it is not affected by the spin direction, similar to Mn₃XN ($X = \text{Ga, Zn, Ag, or Ni}$) [39]. On the other hand, σ_{xy}^2 plotted in Fig. 3(d) oscillates drastically in the low-energy region and tends to zero above 5.5 eV. The positive and negative values of σ_{xy}^2 indicate that the interband transitions are dominated by the excitations caused by the left- and right-circularly polarized light, respectively. The signs of σ_{xy}^2 for the states of $S(90^\circ, 30^\circ)$ and $S(90^\circ, 90^\circ)$ are opposite, which has the same physical mechanism as the intrinsic AHC for monolayer LaCl [69]. The simple reason is that the states of $S(90^\circ, 30^\circ)$ and $S(90^\circ, 90^\circ)$ are related to each other by a combined symmetry $\mathcal{M}_y C_{6z}$, which changes the sign of the optical Hall conductivity, i.e., $\mathcal{M}_y C_{6z} \sigma_{xy} = -\sigma_{xy}$. It should further be noticed that for the state of $S(90^\circ, 0^\circ)$, σ_{xy}^2 is suppressed due to the presence of the mirror plane \mathcal{M} that is perpendicular to S , which is consistent with previous group theory analyses. Utilizing the Kramers-Kronig transformation, the dispersive parts of the optical conductivity, σ_{xx}^2 and σ_{xy}^1 , can be obtained from the corresponding absorptive parts according to Eqs. (3) and (4). The dependence of σ_{xx}^2 and σ_{xy}^1 on the magnetization direction, featured in Figs. 3(b) and 3(c), resemble that of σ_{xx}^1 and σ_{xy}^2 .

Then, we proceed to the out-of-plane magnetization by considering the spin within the yz plane, for example, $S(0^\circ, 90^\circ)$ ($S \parallel z$) and $S(45^\circ, 90^\circ)$. As shown in Figs. 3(e) and 3(f), σ_{xx}^1 has two absorption peaks at 0.6 and 2.2 eV, and meanwhile, σ_{xx}^2 presents two valleys at 0.5 and 2.0 eV.

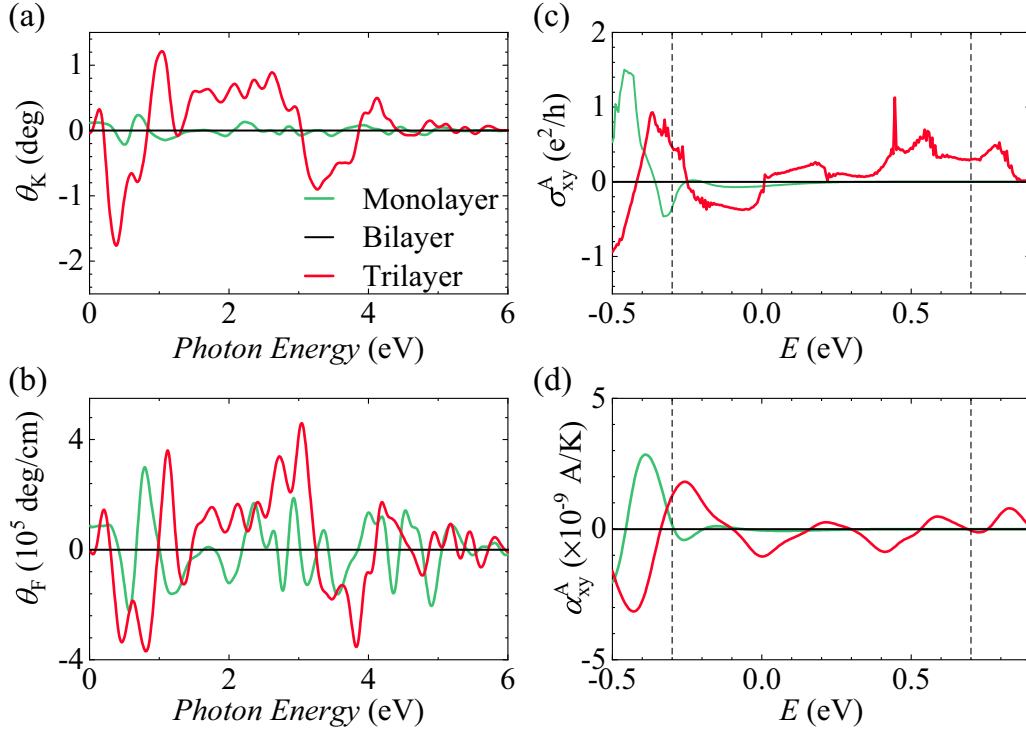


FIG. 9. (a) The Kerr and (b) Faraday rotation angles of bilayer and trilayer 1T-CrTe₂. (c) The anomalous Hall and (d) anomalous Nernst conductivities of bilayer and trilayer 1T-CrTe₂ as a function of the Fermi energy. The magnetization direction is along the y axis. For a better comparison, the curves of monolayer 1T-CrTe₂ are also plotted. The vertical dashed lines in (c) and (d) mark the realistic doping region of -0.31 to 0.70 eV.

This is identical to the situation for in-plane magnetization and further indicates that the diagonal elements of optical conductivity are not affected by the spin direction. In contrast, the off-diagonal elements of optical conductivity, σ_{xy}^1 and σ_{xy}^2 [see Figs. 3(g) and 3(h)], obviously depend on the spin direction. σ_{xy}^1 and σ_{xy}^2 oscillate as a function of photon energy with different spin directions and reach the maximal values when the spin points towards the z axis. It is important to notice that the off-diagonal elements of optical conductivity with out-of-plane magnetization are enhanced by about one order of magnitude compared to those with in-plane magnetization.

Now, we present the magneto-optical Kerr and Faraday spectra with in-plane and out-of-plane magnetization, as shown in Figs. 4 and 5, respectively. The Kerr and Faraday spectra are rather similar to that of σ_{xy} , and the reason can be simply attributed to their close relationships [refer to Eqs. (5) and (7)]. For the in-plane magnetization, the Kerr and Faraday angles are vanishing if the spin points along $\varphi = n\pi/3$, for example, $\varphi = 0^\circ$ [see Figs. 4(a)–4(d)], due to the symmetry restriction. When the spin rotates to $\varphi = \pi/6 + n\pi/3$, the Kerr and Faraday angles reach their maxima, that is, $\theta_K^{\max} = 0.24^\circ$ and $\theta_F^{\max} = (3.00 \times 10^5)^\circ/\text{cm}$ at the photon energies of 0.70 and 0.79 eV, respectively. The θ_K^{\max} of CrTe₂ is comparable to the Kerr rotation angles of monolayer CrI₃ (0.286°) [12] and of blue phosphorene (0.12°) [70]. Moreover, Figs. 4(e)–4(h) show that the maximal Kerr and Faraday angles of monolayer CrTe₂ exhibit a period of $2\pi/3$ when the spin rotates within the xy plane.

On the other hand, the Kerr and Faraday spectra with out-of-plane magnetization are illustrated in Fig. 5. As a result of the off-diagonal elements of optical conductivity, the Kerr and Faraday spectra with out-of-plane magnetization are significantly stronger than those with in-plane magnetization [Figs. 5(a)–5(d)]. The maximal Kerr and Faraday rotation angles appear when $\theta = 0^\circ$ ($S \parallel z$), that is, $\theta_K^{\max} = -1.34^\circ$ and $\theta_F^{\max} = -(17.30 \times 10^5)^\circ/\text{cm}$ at photon energies of 0.66 and 0.82 eV, respectively. Moreover, the Kerr and Faraday angles have a period of 2π as a function of polar angle θ , as shown in Figs. 5(e)–5(h), demonstrating again that the MOE can be effectively modulated by tuning the spin direction.

4. Anomalous Hall and anomalous Nernst effects

As mentioned above, the dc limit of real off-diagonal element of optical conductivity, i.e., $\sigma_{xy}^1(\omega \rightarrow 0)$, is nothing but the AHC σ_{xy}^A , which can be alternatively evaluated by integrating the Berry curvature over the entire Brillouin zone [see Eq. (8)] [55]. Figure 6(a) plots the AHC as a function of the Fermi energy when the spin points along the x, y, and z axes. σ_{xy}^A is vanishing when $S \parallel x$ and begins to appear if $S \parallel y$ and z , indicating the same symmetry requirements for the MOE. In analogy to the Kerr and Faraday angles, σ_{xy}^A with out-of-plane magnetization ($S \parallel z$) is significantly larger than that with in-plane magnetization ($S \parallel y$). Thus, at the actual Fermi energy, σ_{xy}^A with both in-plane and out-of-plane magnetizations are relatively small, which is difficult to measure experimentally. Nevertheless, the pronounced peaks of AHC arise after appropriate electrons or holes (h) are introduced.

TABLE III. The magneto-optical Kerr rotation angle θ_K , anomalous Hall conductivity σ_{xy}^A , and anomalous Nernst conductivity α_{xy}^A for CrTe₂ and other 2D magnetic materials. The results of CrTe₂ are obtained at the magnetic ground states with the spin pointing along the y axis. BP and GA stand for blue phosphorene and gray arsenene, respectively, which are metallic ferromagnets under hole doping [70], similar to the case of InS [54]. ML, BL, and TL indicate monolayer, bilayer, and trilayer, respectively. For a better comparison, the units of anomalous Hall (Nernst) conductivity for CrTe₂ are given by both e^2/h (A/K) and S/cm (A/mK), which can be converted to each other via the effective thicknesses of ML (6.23 Å) and TL (18.69 Å).

	θ_K (deg)	
CrTe ₂	0.24 (ML), -1.76 (TL)	
CrI ₃ [12]	0.29 (ML), 2.86 (TL)	
BP, GA [70]	0.12, 0.81 (ML), 0.03, 0.14 (BL)	
InS [54]	0.34 (ML)	
Cr ₂ Ge ₂ Te ₆ [74]	0.9 (ML), 1.5 (BL), 2.2 (TL)	
	σ_{xy}^A	α_{xy}^A
CrTe ₂ (e^2/h , 10^{-9} A/K)	-0.34 (ML), 1.13 (TL)	-0.42 (ML), 1.80 (TL)
CrTe ₂ (S/cm, A/mK)	-210.89 (ML), 234.66 (TL)	-0.67 (ML), 0.97 (TL)
Fe ₃ GeTe ₂ (S/cm, A/mK) [75]	360 ~ 400 (20–40 nm)	~0.3 (20–40 nm)
Fe ₄ GeTe ₂ (S/cm, A/mK) [76]	~180 (11-layer)	
FeCl ₂ (S/cm, A/mK) [77]		0.35 (ML)

Considering the fact that the doping concentration for 2D metallic materials, such as 1T-TiSe₂ [71], has recorded up to $1 \times 10^{15} \text{ cm}^{-2}$, the realistic doping region for CrTe₂ is estimated to be -0.31 to 0.70 eV. Within this energy range, σ_{xy}^A can increase up to $0.33 e^2/h$ at 0.50 eV when $S \parallel z$ and up to $-0.34 e^2/h$ at -0.30 eV when $S \parallel y$. When the spin rotates within the xy and yz planes, σ_{xy}^A exhibits periods of $2\pi/3$ and 2π , respectively [depicted in Figs. 6(b) and 6(c)], which are identical to the behaviors of Kerr and Faraday angles.

The ANE, being regarded as the thermoelectric counterpart of the AHE, is a celebrated effect from the realm of spin caloritronics [72,73]. The conclusions of symmetry analyses for the AHE are also applicable to the ANE, according to Eqs. (8) and (10). That is, the ANC α_{xy}^A is forbidden when the spin is along $\varphi = n\pi/3$, e.g., $S \parallel x$, and becomes nonzero if $S \parallel y$ or z , as clearly shown in Fig. 6(d). Due to the high Curie temperature of CrTe₂ ($T_C > 300$ K) [30–32], the first-principles calculations of the ANC are carried out at a temperature of 300 K. Similar to the AHC σ_{xy}^A , the ANC α_{xy}^A with out-of-plane magnetization ($S \parallel z$) is evidently larger than that with in-plane magnetization ($S \parallel y$). For both in-plane and out-of-plane magnetizations, α_{xy}^A are almost zero at the actual Fermi energy and give rise to pronounced peaks by electron or hole doping. For example, α_{xy}^A reaches up to 1.12×10^{-9} A/K at -0.30 eV when $S \parallel z$ and up to -0.42×10^{-9} A/K at -0.26 eV when $S \parallel y$. Moreover, α_{xy}^A displays a period of $2\pi/3$ (2π) when the spin rotates within the xy (yz) plane, as shown in Figs. 6(e) and 6(f), just like the AHC and the Kerr and Faraday angles.

B. Multilayer CrTe₂

In this section, we shall discuss the layer-dependent magnetic properties as well as the MOE, AHE, and ANE of multilayer CrTe₂. Bilayer and trilayer CrTe₂ with the AA-stacking pattern, which could be directly exfoliated from the bulk structure, is considered here. To determine the magnetic ground states, we calculate the total energy E_{tot} of in-plane

and out-of-plane ferromagnetic and antiferromagnetic structures, as depicted in Fig. 7. It should be stressed here that all the trilayer CrTe₂ structures are actually ferromagnetic with finite net magnetization, while we mention the “antiferromagnetic” trilayer structures [Figs. 7(f) and 7(h)] just because of the interlayer antiferromagnetic order. The energy results are summarized in Table II, from which one can find that the antiferromagnetic structures for both bilayer [Figs. 7(b) and 7(d)] and trilayer [Figs. 7(f) and 7(h)] CrTe₂ are energetically favorable. Thus, the in-plane antiferromagnetic structures [Figs. 7(b) and 7(f)] are most stable with energies of ~ 4 and ~ 1 meV/cell, slightly lower than those of the out-of-plane ones for bilayer and trilayer, respectively. We should note that in two recent experimental works [31,32], the interlayer antiferromagnetic order was not explicitly evidenced as the thinnest sample with a thickness of five single layers loses the signal of in-plane magnetism. In the following, we focus on only bilayer and trilayer CrTe₂ with in-plane antiferromagnetic structures. The electronic band structures plotted in Fig. 8 demonstrate the metallic nature of both bilayer and trilayer CrTe₂.

Using group theory, we analyze whether the MOE, AHE, and ANE can exist in bilayer and trilayer CrTe₂. The magnetic point group of the in-plane antiferromagnetic bilayer [Fig. 7(b)] is $2'/m'$, which contains the space-time inversion symmetry \mathcal{TP} that forbids any signals of magneto-optical responses as well as anomalous charge and thermoelectric transport. In contrast, the magnetic point group of the in-plane antiferromagnetic trilayer [Fig. 7(f)] is the same as that of monolayer CrTe₂, i.e., $2'/m'$, which allows the presence of the MOE, AHE, and ANE.

The layer number can influence the MOE, AHE, and ANE of multilayer CrTe₂. The magneto-optical Kerr and Faraday rotation angles of in-plane antiferromagnetic bilayer and trilayer CrTe₂ are plotted in Figs. 9(a) and 9(b), in which the results of monolayer CrTe₂ are given for comparison. As expected, θ_K and θ_F of the bilayer structure are zero due to the presence of \mathcal{TP} symmetry. For the trilayer structure, the largest θ_K and θ_F are -1.76° and $(4.60 \times 10^5)^\circ/\text{cm}$ at

photon energies of 0.38 and 3.04 eV, respectively. One can find that the Kerr and Faraday effects of the trilayer structure are generally stronger than those of the monolayer structure. Moreover, the AHC and ANC of monolayer, bilayer, and trilayer CrTe₂ with in-plane magnetization are presented in Figs. 9(c) and 9(d), respectively. Clearly, σ_{xy}^A and α_{xy}^A of the bilayer structure are vanishing due to the symmetry restriction. σ_{xy}^A and α_{xy}^A of the trilayer structure are $-0.11 e^2/h$ and $-1.05 \times 10^{-9} \text{ A/K}$ at the actual Fermi energy. After introducing appropriate holes or electrons, σ_{xy}^A and α_{xy}^A can increase up to $1.13 e^2/h$ at 0.45 eV and $1.80 \times 10^{-9} \text{ A/K}$ at -0.26 eV , respectively. The AHE and ANE of the trilayer structure are overall larger than those of the monolayer structure.

IV. SUMMARY

In summary, using first-principles density functional theory calculations and group theory analyses, we have systematically investigated the electronic, magnetic, magneto-optical, anomalous charge, and thermoelectric transport properties of monolayer, bilayer, and trilayer 1T-CrTe₂. The monolayer is a ferromagnetic metal with the in-plane magnetization along the y axis. The in-plane magnetocrystalline anisotropy energy is as small as $10 \mu\text{eV/cell}$, indicating that the spin can be easily rotated within the xy plane. The magneto-optical Kerr and Faraday rotation angles as well as anomalous Hall and Nernst conductivities exhibit a period of $2\pi/3$ when the spin rotates within the xy plane, and their maxima of $\theta_K = 0.24^\circ$, $\theta_F = (3.00 \times 10^5)^\circ/\text{cm}$, $\sigma_{xy}^A = -0.34 e^2/h$, and $\alpha_{xy}^A = -0.42 \times 10^{-9} \text{ A/K}$ (300 K) appear at $\varphi = n\pi/3 + \pi/6$, with $n \in \mathbb{N}$. At the azimuthal angle $\varphi = n\pi/3$, the mirror planes that are normal to the spin direction suppress the magneto-optical, anomalous Hall, and anomalous Nernst effects. If the spin cants from the in-plane to out-of-plane direction, the magneto-optical, anomalous Hall, and anomalous Nernst effects are significantly enhanced, and particularly, they reach the maximal values of $\theta_K = -1.34^\circ$, $\theta_F = (-17.30 \times 10^5)^\circ/\text{cm}$, $\sigma_{xy}^A = 0.33 e^2/h$, and $\alpha_{xy}^A = 1.12 \times 10^{-9} \text{ A/K}$ (300 K) when the spin is along the z axis (i.e., polar angle $\theta = 0^\circ$). The bilayer 1T-CrTe₂ prefers an in-plane antiferromagnetic structure with the magnetization along the y axis, which has a space-time inversion symmetry \mathcal{TP} that prohibits the signals of magneto-optical responses as well as anomalous Hall and Nernst transports. The trilayer 1T-CrTe₂ is also inclined

to the in-plane antiferromagnetic order between two adjacent layers but has finite net magnetization due to the odd number of layers. The magnetic point group of trilayer structure with in-plane antiferromagnetic order is identical to that of monolayer structure and thus allows the presence of all the physical phenomena mentioned above. In particular, the magneto-optical Kerr and Faraday rotation angles as well as anomalous Hall and anomalous Nernst conductivities of the trilayer structure are obviously larger than those of the monolayer structure with the magnetization along the y axis. For example, the maximal values of $\theta_K = -1.76^\circ$, $\theta_F = (4.60 \times 10^5)^\circ/\text{cm}$, $\sigma_{xy}^A = 1.13 e^2/h$, and $\alpha_{xy}^A = 1.80 \times 10^{-9} \text{ A/K}$ (300 K) are found in the trilayer structure. Our results suggest that the magneto-optical, anomalous Hall, and anomalous Nernst effects for two-dimensional room-temperature ferromagnet 1T-CrTe₂ can be effectively modulated by altering the magnetization direction and layer number.

The magnitudes of magneto-optical, anomalous Hall, and anomalous Nernst effects for 1T-CrTe₂ are comparable to or even larger than those of other 2D magnetic materials. As listed in Table III, the Kerr rotation angle of CrTe₂ is larger than that of blue phosphorene (BP) and gray arsenene (GA) [70] and is comparable to that of CrI₃ [12], InS [54], and Cr₂Ge₂Te₆ [74]. The large magneto-optical Kerr rotation angle appearing in CrTe₂ suggests that it is a promising 2D material platform for the applications of magneto-optical devices. Although the anomalous Hall and anomalous Nernst conductivities of CrTe₂ at the actual Fermi energy is not significant, greater values can be obtained by hole or electron doping. The obtained anomalous Hall conductivity is smaller and larger than those of Fe₃GeTe₂ [75] and Fe₄GeTe₂ [76], respectively, while the anomalous Nernst conductivity of trilayer CrTe₂ is significantly larger than that of Fe₃GeTe₂ [75] and FeCl₂ [77]. Our results also suggest that the 2D room-temperature ferromagnet CrTe₂ can be potentially used for spintronics and spin caloritronics devices.

ACKNOWLEDGMENTS

W.F. and Y.Y. acknowledge the support from the National Natural Science Foundation of China (Grants No. 11874085 and No. 11734003) and the National Key R&D Program of China (Grant No. 2016YFA0300600). X.Z. acknowledges the support from the Graduate Technological Innovation Project of Beijing Institute of Technology (Grant No. 2019CX10018).

- [1] C. Gong and X. Zhang, Two-dimensional magnetic crystals and emergent heterostructure devices, *Science* **363**, eaav4450 (2019).
- [2] N. D. Mermin and H. Wagner, Absence of Ferromagnetism or Antiferromagnetism in One-or Two-Dimensional Isotropic Heisenberg Models, *Phys. Rev. Lett.* **17**, 1133 (1966).
- [3] F. Hellman *et al.*, Interface-induced phenomena in magnetism, *Rev. Mod. Phys.* **89**, 025006 (2017).
- [4] K. S. Burch, D. Mandrus, and J.-G. Park, Magnetism in two-

dimensional van der Waals materials, *Nature (London)* **563**, 47 (2018).

- [5] B. Sachs, T. O. Wehling, K. S. Novoselov, A. I. Lichtenstein, and M. I. Katsnelson, Ferromagnetic two-dimensional crystals: Single layers of K₂CuF₄, *Phys. Rev. B* **88**, 201402(R) (2013).
- [6] J.-G. Park, Opportunities and challenges of two-dimensional magnetic van der Waals materials: Magnetic graphene? *J. Phys.: Condens. Matter* **28**, 301001 (2016).

- [7] D. Zhong, K. L. Seyler, X. Linpeng, R. Cheng, N. Sivadas, B. Huang, E. Schmidgall, T. Taniguchi, K. Watanabe, M. A. McGuire, W. Yao, D. Xiao, K.-M. C. Fu, and X. Xu, Van der Waals engineering of ferromagnetic semiconductor heterostructures for spin and valleytronics, *Sci. Adv.* **3**, e1603113 (2017).
- [8] N. Samarth, Condensed-matter physics: Magnetism in flatland, *Nature (London)* **546**, 216 (2017).
- [9] J.-U. Lee, S. Lee, J. H. Ryoo, S. Kang, T. Y. Kim, P. Kim, C.-H. Park, J.-G. Park, and H. Cheong, Ising-type magnetic ordering in atomically thin FePS_3 , *Nano Lett.* **16**, 7433 (2016).
- [10] X. Wang, K. Du, Y. Y. F. Liu, P. Hu, J. Zhang, Q. Zhang, M. H. S. Owen, X. Lu, C. K. Gan, P. Sengupta, C. Kloc, and Q. Xiong, Raman spectroscopy of atomically thin two-dimensional magnetic iron phosphorus trisulfide (FePS_3) crystals, *2D Mater.* **3**, 031009 (2016).
- [11] C. Gong, L. Li, Z. Li, H. Ji, A. Stern, Y. Xia, T. Cao, W. Bao, C. Wang, Y. Wang, Z. Q. Qiu, R. J. Cava, S. G. Louie, J. Xia, and X. Zhang, Discovery of intrinsic ferromagnetism in two-dimensional van der Waals crystals, *Nature (London)* **546**, 265 (2017).
- [12] B. Huang, G. Clark, E. Navarro-Moratalla, D. R. Klein, R. Cheng, K. L. Seyler, D. Zhong, E. Schmidgall, M. A. McGuire, D. H. Cobden, W. Yao, D. Xiao, P. Jarillo-Herrero, and X. Xu, Layer-dependent ferromagnetism in a van der Waals crystal down to the monolayer limit, *Nature (London)* **546**, 270 (2017).
- [13] D. R. Klein, D. MacNeill, J. L. Lado, D. Soriano, E. Navarro-Moratalla, K. Watanabe, T. Taniguchi, S. Manni, P. Canfield, J. Fernández-Rossier, and P. Jarillo-Herrero, Probing magnetism in 2D van der Waals crystalline insulators via electron tunneling, *Science* **360**, 1218 (2018).
- [14] S. Jiang, L. Li, Z. Wang, K. F. Mak, and J. Shan, Controlling magnetism in 2D CrI_3 by electrostatic doping, *Nat. Nanotechnol.* **13**, 549 (2018).
- [15] B. Huang, G. Clark, D. R. Klein, D. MacNeill, E. Navarro-Moratalla, K. L. Seyler, N. Wilson, M. A. McGuire, D. H. Cobden, D. Xiao, W. Yao, P. Jarillo-Herrero, and X. Xu, Electrical control of 2D magnetism in bilayer CrI_3 , *Nat. Nanotechnol.* **13**, 544 (2018).
- [16] S. Jiang, J. Shan, and K. F. Mak, Electric-field switching of two-dimensional van der Waals magnets, *Nat. Mater.* **17**, 406 (2018).
- [17] Z. Wang, I. Gutiérrez-Lezama, N. Ubrig, M. Kroner, M. Gibertini, T. Taniguchi, K. Watanabe, A. Imamoğlu, E. Giannini, and A. F. Morpurgo, Very large tunneling magnetoresistance in layered magnetic semiconductor CrI_3 , *Nat. Commun.* **9**, 2516 (2018).
- [18] N. Sivadas, S. Okamoto, X. Xu, C. J. Fennie, and D. Xiao, Stacking-dependent magnetism in bilayer CrI_3 , *Nano Lett.* **18**, 7658 (2018).
- [19] M. Kim, P. Kumaravadivel, J. Birkbeck, W. Kuang, S. G. Xu, D. G. Hopkinson, J. Knolle, P. A. McClarty, A. I. Berdyugin, M. Ben Shalom, R. V. Gorbachev, S. J. Haigh, S. Liu, J. H. Edgar, K. S. Novoselov, I. V. Grigorieva, and A. K. Geim, Micromagnetometry of two-dimensional ferromagnets, *Nat. Electron.* **2**, 457 (2019).
- [20] D. R. Klein, D. MacNeill, Q. Song, D. T. Larson, S. Fang, M. Xu, R. A. Ribeiro, P. C. Canfield, E. Kaxiras, R. Comin, and P. Jarillo-Herrero, Enhancement of interlayer exchange in an ultrathin two-dimensional magnet, *Nat. Phys.* **15**, 1255 (2019).
- [21] H. H. Kim, B. Yang, S. Li, S. Jiang, C. Jin, Z. Tao, G. Nichols, F. Sfigakis, S. Zhong, C. Li, S. Tian, D. G. Cory, G.-X. Miao, J. Shan, K. F. Mak, H. Lei, K. Sun, L. Zhao, and A. W. Tsen, Evolution of interlayer and intralayer magnetism in three atomically thin chromium trihalides, *Proc. Natl. Acad. Sci. USA* **116**, 11131 (2019).
- [22] Y. Deng, Y. Yu, Y. Song, J. Zhang, N. Z. Wang, Z. Sun, Y. Yi, Y. Z. Wu, S. Wu, J. Zhu, J. Wang, X. H. Chen, and Y. Zhang, Gate-tunable room-temperature ferromagnetism in two-dimensional Fe_3GeTe_2 , *Nature (London)* **563**, 94 (2018).
- [23] Z. Fei, B. Huang, P. Malinowski, W. Wang, T. Song, J. Sanchez, W. Yao, D. Xiao, X. Zhu, A. F. May, W. Wu, D. H. Cobden, J.-H. Chu, and X. Xu, Two-dimensional itinerant ferromagnetism in atomically thin Fe_3GeTe_2 , *Nat. Mater.* **17**, 778 (2018).
- [24] J.-M. Xu, S.-Y. Wang, W.-J. Wang, Y.-H. Zhou, X.-L. Chen, Z.-R. Yang, and Z. Qu, Possible tricritical behavior and anomalous lattice softening in van der Waals itinerant ferromagnet Fe_3GeTe_2 under high pressure, *Chin. Phys. Lett.* **37**, 076202 (2020).
- [25] M. Bonilla, S. Kolekar, Y. Ma, H. C. Diaz, V. Kalappattil, R. Das, T. Eggers, H. R. Gutierrez, M.-H. Phan, and M. Batzill, Strong room-temperature ferromagnetism in VSe_2 monolayers on van der Waals substrates, *Nat. Nanotechnol.* **13**, 289 (2018).
- [26] J. Li, B. Zhao, P. Chen, R. Wu, B. Li, Q. Xia, G. Guo, J. Luo, K. Zang, Z. Zhang, H. Ma, G. Sun, X. Duan, and X. Duan, Synthesis of Ultrathin Metallic MTe_2 ($M = \text{V}, \text{Nb}, \text{Ta}$) single-crystalline nanoplates, *Adv. Mater.* **30**, 1801043 (2018).
- [27] D. J. O'Hara, T. Zhu, A. H. Trout, A. S. Ahmed, Y. K. Luo, C. H. Lee, M. R. Brenner, S. Rajan, J. A. Gupta, D. W. McComb, and R. K. Kawakami, Room temperature intrinsic ferromagnetism in epitaxial manganese selenide films in the monolayer limit, *Nano Lett.* **18**, 3125 (2018).
- [28] Q.-Q. Yuan, Z. Guo, Z.-Q. Shi, H. Zhao, Z.-Y. Jia, Q. Wang, J. Sun, D. Wu, and S.-C. Li, Ferromagnetic MnSn Monolayer Epitaxially Grown on Silicon Substrate, *Chin. Phys. Lett.* **37**, 077502 (2020).
- [29] A. Avsar, A. Ciarrocchi, M. Pizzochero, D. Unuchek, O. V. Yazyev, and A. Kis, Defect induced, layer-modulated magnetism in ultrathin metallic PtSe_2 , *Nat. Nanotechnol.* **14**, 674 (2019).
- [30] D. C. Freitas, R. Weht, A. Sulpice, G. Remenyi, P. Strobel, F. Gay, J. Marcus, and M. Núñez-Regueiro, Ferromagnetism in layered metastable 1T-CrTe_2 , *J. Phys.: Condens. Matter* **27**, 176002 (2015).
- [31] X. Sun *et al.*, Room temperature ferromagnetism in ultra-thin van der Waals crystals of 1T-CrTe_2 , *Nano Res.* **13**, 3358 (2020).
- [32] A. Purbawati, J. Coraux, J. Vogel, A. Hadj-Azzem, N. Wu, N. Bendjab, D. Jegouso, J. Renard, L. Marty, V. Bouchiat, A. Sulpice, L. Aballe, M. Foerster, F. Genuzio, A. Locatelli, T. O. Montes, Z. V. Han, X. Sun, M. Núñez-Regueiro, and N. Rougemaille, In-plane magnetic domains and Néel-like domain walls in thin flakes of the room temperature CrTe_2 van der Waals ferromagnet, *ACS Appl. Mater. Interfaces* **12**, 30702 (2020).
- [33] J. Kerr, On rotation of the plane of polarization by reflection from the pole of a magnet, *Philos. Mag.* **3**, 321 (1877).
- [34] M. Faraday, Experimental researches in electricity.—Nineteenth series, *Philos. Trans. R. Soc. London* **136**, 1 (1846).
- [35] V. Antonov, B. Harmon, and A. Yaresko, *Electronic Structure*

- and *Magneto-optical Properties of Solids* (Kluwer, Dordrecht, The Netherlands, 2004).
- [36] N. Nagaosa, J. Sinova, S. Onoda, A. H. MacDonald, and N. P. Ong, Anomalous Hall effect, *Rev. Mod. Phys.* **82**, 1539 (2010).
 - [37] R. Kubo, Statistical-mechanical theory of irreversible processes. I. General theory and simple applications to magnetic and conduction problems, *J. Phys. Soc. Jpn.* **12**, 570 (1957).
 - [38] C. S. Wang and J. Callaway, Band structure of nickel: Spin-orbit coupling, the Fermi surface, and the optical conductivity, *Phys. Rev. B* **9**, 4897 (1974).
 - [39] X. Zhou, J.-P. Hanke, W. Feng, F. Li, G.-Y. Guo, Y. Yao, S. Blügel, and Y. Mokrousov, Spin-order dependent anomalous Hall effect and magneto-optical effect in the noncollinear antiferromagnets Mn_3XN with $\text{X} = \text{Ga, Zn, Ag, or Ni}$, *Phys. Rev. B* **99**, 104428 (2019).
 - [40] W. Nernst, Ueber die electromotorischen Kräfte, welche durch den Magnetismus in von einem Wärmestrome durchflossenen Metallplatten geweckt werden, *Ann. Phys. (Berlin, Ger.)* **267**, 760 (1887).
 - [41] N. Hanasaki, K. Sano, Y. Onose, T. Ohtsuka, S. Iguchi, I. Kézsmárki, S. Miyasaka, S. Onoda, N. Nagaosa, and Y. Tokura, Anomalous Nernst Effects in Pyrochlore Molybdates with Spin Chirality, *Phys. Rev. Lett.* **100**, 106601 (2008).
 - [42] M. Ikhlas, T. Tomita, T. Koretsune, M.-T. Suzuki, D. Nishio-Hamane, R. Arita, Y. Otani, and S. Nakatsuji, Large anomalous Nernst effect at room temperature in a chiral antiferromagnet, *Nat. Phys.* **13**, 1085 (2017).
 - [43] T. Liang, J. Lin, Q. Gibson, T. Gao, M. Hirschberger, M. Liu, R. J. Cava, and N. P. Ong, Anomalous Nernst Effect in the Dirac Semimetal Cd_3As_2 , *Phys. Rev. Lett.* **118**, 136601 (2017).
 - [44] C. Wuttke, F. Caglieris, S. Sykora, F. Scaravaggi, A. U. B. Wolter, K. Manna, V. Süß, C. Shekhar, C. Felser, B. Büchner, and C. Hess, Berry curvature unravelled by the anomalous Nernst effect in Mn_3Ge , *Phys. Rev. B* **100**, 085111 (2019).
 - [45] G. Kresse and J. Hafner, *Ab initio* molecular dynamics for liquid metals, *Phys. Rev. B* **47**, 558 (1993).
 - [46] G. Kresse and J. Furthmüller, Efficient iterative schemes for *ab initio* total-energy calculations using a plane-wave basis set, *Phys. Rev. B* **54**, 11169 (1996).
 - [47] P. E. Blöchl, Projector augmented-wave method, *Phys. Rev. B* **50**, 17953 (1994).
 - [48] J. P. Perdew, K. Burke, and M. Ernzerhof, Generalized Gradient Approximation Made Simple, *Phys. Rev. Lett.* **77**, 3865 (1996).
 - [49] V. I. Anisimov, J. Zaanen, and O. K. Andersen, Band theory and Mott insulators: Hubbard U instead of Stoner I , *Phys. Rev. B* **44**, 943 (1991).
 - [50] S. L. Dudarev, G. A. Botton, S. Y. Savrasov, C. J. Humphreys, and A. P. Sutton, Electron-energy-loss spectra and the structural stability of nickel oxide: An LSDA+ U study, *Phys. Rev. B* **57**, 1505 (1998).
 - [51] X. Sui, T. Hu, J. Wang, B.-L. Gu, W. Duan, and M.-s. Miao, Voltage-controllable colossal magnetocrystalline anisotropy in single-layer transition metal dichalcogenides, *Phys. Rev. B* **96**, 041410(R) (2017).
 - [52] A. A. Mostofi, J. R. Yates, Y.-S. Lee, I. Souza, D. Vanderbilt, and N. Marzari, wannier90: A tool for obtaining maximally-localised Wannier functions, *Comput. Phys. Commun.* **178**, 685 (2008).
 - [53] J. Callaway, *Quantum Theory of the Solid State* (Academic Press, San Diego, 1991).
 - [54] W. Feng, G.-Y. Guo, and Y. Yao, Tunable magneto-optical effects in hole-doped group-IIIA metal-monochalcogenide monolayers, *2D Mater.* **4**, 015017 (2017).
 - [55] Y. Yao, L. Kleinman, A. H. MacDonald, J. Sinova, T. Jungwirth, D.-s. Wang, E. Wang, and Q. Niu, First Principles Calculation of Anomalous Hall Conductivity in Ferromagnetic bcc Fe, *Phys. Rev. Lett.* **92**, 037204 (2004).
 - [56] D. Xiao, Y. Yao, Z. Fang, and Q. Niu, Berry-Phase Effect in Anomalous Thermoelectric Transport, *Phys. Rev. Lett.* **97**, 026603 (2006).
 - [57] X. Zhou, J.-P. Hanke, W. Feng, S. Blügel, Y. Mokrousov, and Y. Yao, Giant anomalous Nernst effect in noncollinear antiferromagnetic Mn-based antiperovskite nitrides, *Phys. Rev. Materials* **4**, 024408 (2020).
 - [58] P. W. Anderson, Antiferromagnetism. Theory of superexchange interaction, *Phys. Rev.* **79**, 350 (1950).
 - [59] J. B. Goodenough, An interpretation of the magnetic properties of the perovskite-type mixed crystals $\text{La}_{1-x}\text{Sr}_x\text{CoO}_{3-x}$, *J. Phys. Chem. Solids* **6**, 287 (1958).
 - [60] J. Kanamori, Superexchange interaction and symmetry properties of electron orbitals, *J. Phys. Chem. Solids* **10**, 87 (1959).
 - [61] H. Y. Lv, W. J. Lu, D. F. Shao, Y. Liu, and Y. P. Sun, Strain-controlled switch between ferromagnetism and antiferromagnetism in $1T\text{-CrX}_2$ ($\text{X} = \text{Se, Te}$) monolayers, *Phys. Rev. B* **92**, 214419 (2015).
 - [62] X. Lu, R. Fei, L. Zhu, and L. Yang, Meron-like topological spin defects in monolayer CrCl_3 , *Nat. Commun.* **11**, 4724 (2020).
 - [63] A. Bedoya-Pinto, J.-R. Ji, A. Pandeya, P. Gargiani, M. Valdivares, P. Sessi, F. Radu, K. Chang, and S. Parkin, Intrinsic 2D-XY ferromagnetism in a van der Waals monolayer, [arXiv:2006.07605](https://arxiv.org/abs/2006.07605).
 - [64] C. Song, X. Liu, X. Wu, J. Wang, J. Pan, T. Zhao, C. Li, and J. Wang, Surface-vacancy-induced metallicity and layer-dependent magnetic anisotropy energy in $\text{Cr}_2\text{Ge}_2\text{Te}_6$, *J. Appl. Phys.* **126**, 105111 (2019).
 - [65] W.-B. Zhang, Q. Qu, P. Zhu, and C.-H. Lam, Robust intrinsic ferromagnetism and half semiconductivity in stable two-dimensional single-layer chromium trihalides, *J. Mater. Chem. C* **3**, 12457 (2015).
 - [66] H. L. Zhuang, P. R. C. Kent, and R. G. Hennig, Strong anisotropy and magnetostriction in the two-dimensional Stoner ferromagnet Fe_3GeTe_2 , *Phys. Rev. B* **93**, 134407 (2016).
 - [67] S. Li, S.-S. Wang, B. Tai, W. Wu, B. Xiang, X.-L. Sheng, and S. A. Yang, Tunable anomalous Hall transport in bulk and two-dimensional $1T\text{-CrTe}_2$: A first-principles study, *Phys. Rev. B* **103**, 045114 (2021).
 - [68] H. T. Stokes, D. M. Hatch, and B. J. Campbell, ISOTROPY software suite, <https://stokes.byu.edu/iso/isotropy.php>.
 - [69] Z. Liu, G. Zhao, B. Liu, Z. F. Wang, J. Yang, and F. Liu, Intrinsic Quantum Anomalous Hall Effect with In-Plane Magnetization: Searching Rule and Material Prediction, *Phys. Rev. Lett.* **121**, 246401 (2018).
 - [70] X. Zhou, W. Feng, F. Li, and Y. Yao, Large magneto-optical effects in hole-doped blue phosphorene and gray arsenene, *Nanoscale* **9**, 17405 (2017).
 - [71] L. J. Li, E. C. T. O'Farrell, K. P. Loh, G. Eda, B. Özyilmaz, and A. H. C. Neto, Controlling many-body states by the electric-

- field effect in a two-dimensional material, [Nature \(London\)](#) **529**, 185 (2016).
- [72] G. E. W. Bauer, E. Saitoh, and B. J. van Wees, Spin caloritronics, [Nat. Mater.](#) **11**, 391 (2012).
- [73] S. R. Boona, R. C. Myers, and J. P. Heremans, Spin caloritronics, [Energy Environ. Sci.](#) **7**, 885 (2014).
- [74] Y. Fang, S. Wu, Z.-Z. Zhu, and G.-Y. Guo, Large magneto-optical effects and magnetic anisotropy energy in two-dimensional $\text{Cr}_2\text{Ge}_2\text{Te}_6$, [Phys. Rev. B](#) **98**, 125416 (2018).
- [75] J. Xu, W. A. Phelan, and C.-L. Chien, Large anomalous Nernst effect in a van der Waals ferromagnet Fe_3GeTe_2 , [Nano Lett.](#) **19**, 8250 (2019).
- [76] J. Seo *et al.*, Nearly room temperature ferromagnetism in a magnetic metal-rich van der Waals metal, [Sci. Adv.](#) **6**, eaay8912 (2020).
- [77] R. Syariati, S. Minami, H. Sawahata, and F. Ishii, First-principles study of anomalous Nernst effect in half-metallic iron dichloride monolayer, [APL Mater.](#) **8**, 041105 (2020).